TRACKING STUDIES IN eRHIC ENERGY-RECOVERY RECIRCULATOR

F. Méot, S. Brooks, V. Ptitsyn, D. Trbojevic, N. Tsoupas
Collider-Accelerator Department, BNL, Upton, NY 11973

Abstract

This paper gives a brief overview of various beam and spin dynamics investigations undertaken in the framework of the design studies regarding the FFAG lattice based electron energy recovery re-circulator ring of the eRHIC electron-ion collider project.

INTRODUCTION

A Fixed Field Alternating Gradient (FFAG) doublet-cell version of the energy recovery recirculator of the eRHIC electron-ion collider [1] is being investigated [2, 3]. A pair of such FFAG rings placed along RHIC recirculate the electron beam through a 1.322 GeV linac (ERL), from respectively 1.3 to 6.6 GeV (5 beams) and 7.9 to 21.2 GeV (11 beams), and back down to injection energy. A spreader and a combiner are placed at the linac ends for proper orbit and 6-D matching, including time-of-flight adjustment.

FFAG LATTICE

The second, 11 beam, 21.2 GeV ring is considered in this discussion since it produces the major SR induced particle and spin dynamics perturbations. The cell is shown in Fig. 1, there are 138 such cells in each one of the 6 eRHIC arcs. The 6 long straight sections (LSS) use that very cell, with quadrupole axes aligned. In the twelve, 17-cell, dispersion suppressors (DS) the quadrupole axes slowly shift from their distance in the arc, to zero at the LSS.

Figure 2 shows the transverse excursion and magnetic field along orbits across the arc cell. Figure 3 shows the energy dependence of the deviation angle and curvature radius in the two quadrupoles, and the energy dependent tunes and chromaticities.

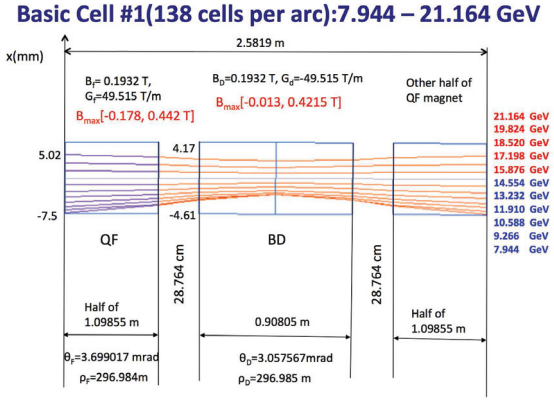

Figure 1 : Arc cell in the 7.944-21.16 GeV recirculating ring.

The y-precession of the spin over the six 138-cell arcs amounts to $6 \times 138 \times a\gamma\theta_{\rm cell} = a\gamma \times (2\pi - 0.688734)$ rad (with the difference to $a\gamma \times 2\pi$ corresponding to the contribution of the 12 DS), *i.e.*, from 18 precessions at 7.944 GeV to 48 at 21.164 GeV. ($a = 0.00116$ is the electron anomalous magnetic factor, γ the Lorentz relativistic factor).

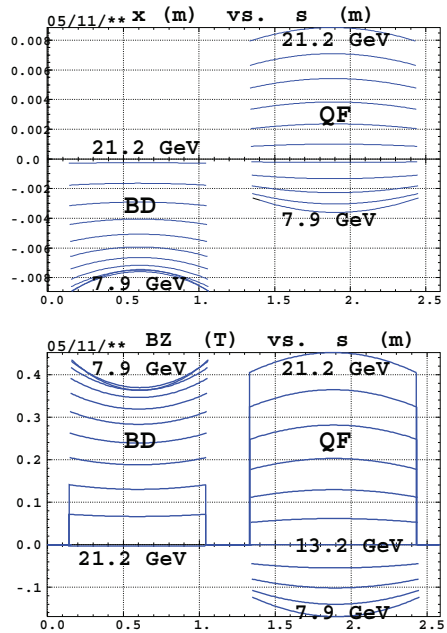

Figure 2: Transverse excursion in the quadrupole frame (hence artefact of trajectory discontinuity) (top) and hard-edged magnetic field (bottom) along the 11 orbits across the arc FFAG cell.

A Note on Dispersion Suppressors

The 12 dispersion suppressors are based on a "missing bend" scheme, where the relative displacement of the two cell quadrupoles (the origin of the dipole effect in the FFAG cell) is brought to zero over a series of cells. From orbit viewpoint, a quadrupole displacement is equivalent to a kick θ_k at entrance and exit [4] (see appendix).

Upon equivalent defect kicks due to the varying displacement of the quads (from their misalignment in the arc to aligned configuration in the straight) the orbit builds along the DS (with origin at upstream arc, end at downstream straight, or reverse) following

$$\frac{x_{\rm orb}(s)}{\sqrt{\beta(s)}} = \frac{x_{\rm orb}(0)}{\sqrt{\beta(0)}}\cos(\phi) + \frac{\alpha(0)x_{\rm orb}(0) + \beta(0)x'_{\rm orb}(0)}{\sqrt{\beta(0)}}\sin(\phi) + \sum_k \sqrt{\beta(s_k)}\theta_k \sin(\phi - \phi_k) \quad (1)$$

$$\frac{\alpha(s)x_{\rm orb}(s) + \beta(s)x'_{\rm orb}(s)}{\sqrt{\beta(s)}} = -\frac{x_{\rm orb}(0)}{\sqrt{\beta(0)}}\sin(\phi) +$$

ISBN 978-3-95450-183-0

$$\frac{\alpha(0)x_{\rm orb}(0)+\beta(0)x'_{\rm orb}(0)}{\sqrt{\beta(0)}}\cos(\phi)+\sum_k\sqrt{\beta(s_k)}\theta_k\cos(\phi-\phi_k)$$

with $x_{\rm orb}(0)$ and $x_{\rm orb}(0)$ the FFAG orbit coordinates in the arc→LSS case, while $x_{\rm orb}(0)=0$, $x'_{\rm orb}(0)=0$ in the LSS→arc case. Figure 4-top shows the orbit build-up from LLS to arc, ending up at the arc with (x,x') coordinates which do not *fully* coincide with the periodic orbit of the arc FFAG cell. The orbit build-up depends on the phase advance $\phi=\int_0^s\frac{ds}{\beta(s)}$, as a consequence it depends on cell tune, and thus on energy. Figure 4-middle shows the resulting orbit build-up in the arcs over 6 consecutive arcs at 5 different energies, 7.9, 9.3, 10.6, 11.9GeV and 13.2 GeV. In each case the starting coordinates (at $s=0$ in the figure, *i.e.*, in the first LSS) are taken $(x,x')=(0,0)$. Figure 4-bottom illustrates the tune dependence of the orbit amplification in the case of pass #4 - for simplicity energy is changed instead of tunes, with the correlation given in Fig. 3.

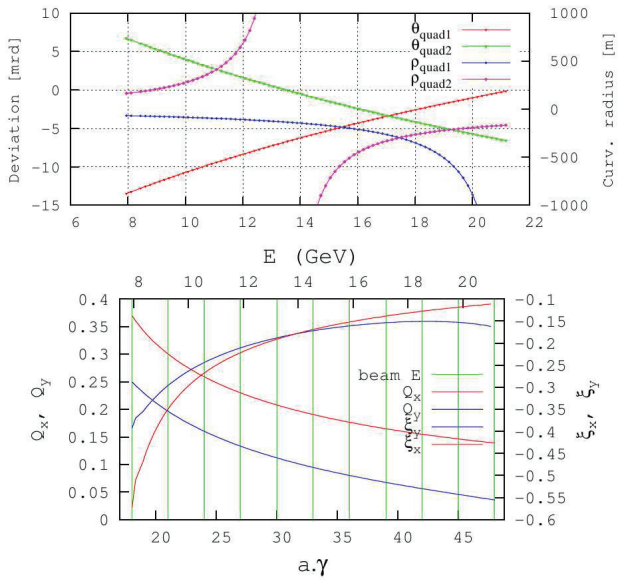

Figure 3: Top : energy dependence of deviation and curvature radius in arc cell quads. Bottom : cell tunes and chromaticities versus energy; the vertical bars materialize the 11 design energies.

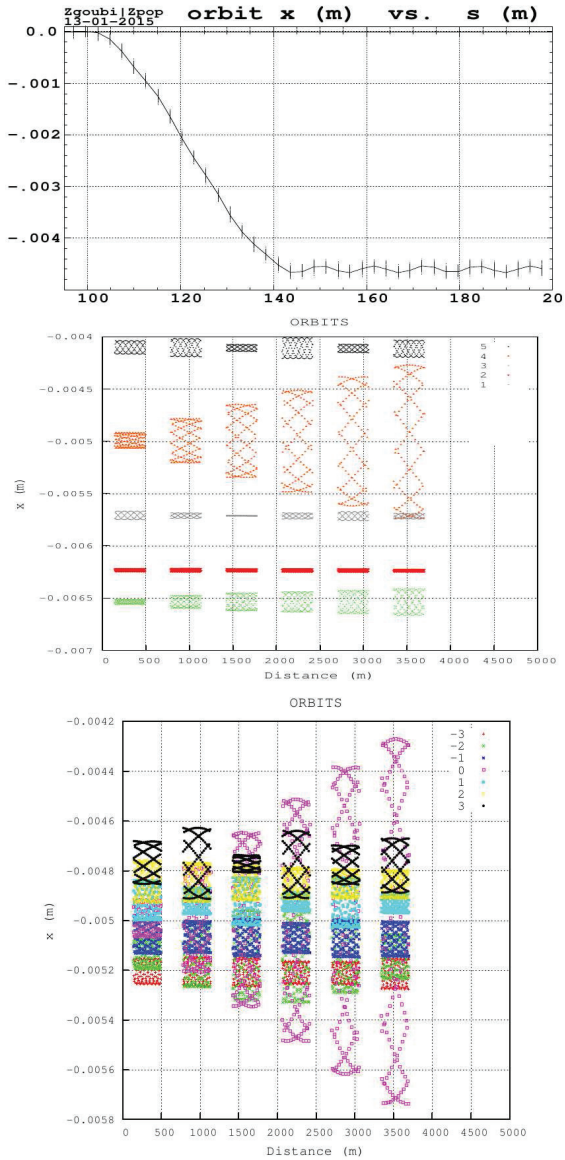

Figure 4: Top : Case of the 11.9GeV pass. The orbit is shown from end of first LSS to upstream region of first arc. Middle : Case of the 11.9GeV pass. The orbit is shown from end of first LSS (from where it starts with zero coordinates) to upstream region of first arc (140-200 m region). Bottom : The orbit is computed for 7 different energies $E+dE$ in the vicinity of $E=11.9$GeV, namely for $dE/E=0,\pm1,2,3\%$. The orbit build-up appears very small for $dE/E=1\%$.

SYNCHROTRON RADIATION

The SR induced energy loss relative to the the bunch centroid and the energy spread write, respectively

$$\frac{\overline{\Delta E}}{E_{\rm ref}}=1.9\times10^{-15}\frac{\gamma^3\Delta\theta}{\rho},\frac{\sigma_E}{E_{\rm ref}}=3.8\times10^{-14}\frac{\gamma^{\frac{5}{2}}\sqrt{\Delta\theta}}{\rho}\quad(2)$$

with $\Delta\theta$ the arc length and $1/\rho$ the curvature, assumed constant. Taking for average radius, in the QF (focusing quad) and BD (defocusing quad) magnets respectively, $\rho_{\rm BD}\approx\frac{s_{\rm BD}}{\Delta\theta_{\rm BD}}$, $\rho_{\rm QF}\approx\frac{s_{\rm QF}}{\Delta\theta_{\rm QF}}$ (with $s_{\rm BD}$ and $s_{\rm QF}$ the arc lengths) and considering in addition, with $l_{\rm BD}$, $l_{\rm QF}$ the magnet lengths, $s_{\rm BD}\approx l_{\rm BD}$, $s_{\rm QF}\approx l_{\rm QF}$, and taking in addition $<(1/\rho)^2>\approx 1/<\rho^2>$, then one gets, per cell

$$\overline{\Delta E}[MeV]\approx0.96\times10^{-15}\gamma^4\left(\frac{l_{\rm BD}}{\rho_{\rm BD}^2}+\frac{l_{\rm QF}}{\rho_{\rm QF}^2}\right)\quad(3)$$

$$\sigma_E\approx1.94\times10^{-14}\gamma^{7/2}\sqrt{\frac{l_{\rm BD}}{|\rho_{\rm BD}^3|}+\frac{l_{\rm QF}}{|\rho_{\rm QF}^3|}}$$

ISBN 978-3-95450-183-0

This is illustrated for a complete eRHIC turn (including LSS and DS sections) in Fig. 5, where it is also compared with Monte Carlo tracking, the agreement is at % level. The energy loss shows a local minimum in the $a\gamma = 30-35$ region, a different behavior from the classical γ^4 dependence in an isomagnetic lattice.

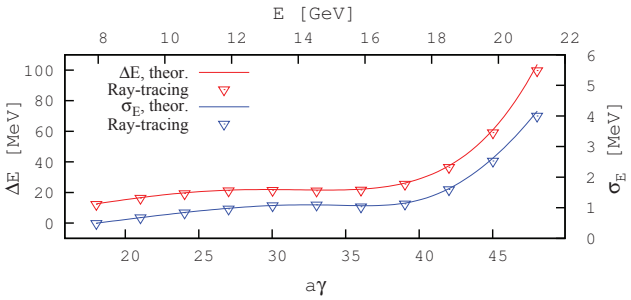

Figure 5: Energy loss and energy spread. Solid lines : theory (Eqs. 3) for a 6-arc ring. Markers : Monte Carlo, for a complete eRHIC ring (see sample tracking outcomes in Fig. 6).

The bunch lengthening over a $[s, s_f]$ distance, resulting from the stochastic energy loss, can be written [5],

$$\sigma_l = \left(\frac{\sigma_E}{E}\right)\left[\frac{1}{L_{\rm bend}}\int_s^{s_f}\left(D_x(s)T_{51}(s_f \leftarrow s) + D'_x(s)T_{52}(s_f \leftarrow s) - T_{56}\right)^2 ds\right]^{1/2} \quad (4)$$

with the integral being taken over the bends, D_x and D'_x the dispersion function and its derivative, T_{5i} the trajectory lengthening coefficient of the first order mapping ($i = 1, 5, 6$ stand for respectively x, δl, $\delta p/p$ coordinates).

The energy loss causes a drift of the bunch centroid, as well as an horizontal emittance increase, both can be computed from the lattice parameters in the linear approximation [5, 6, 7]. Figure 7 illustrates these effects over a 21.164 GeV recirculation (with bunch re-centering on the reference optical axis at each of the six LSS).

Cumulative effect of SR, over a complete 7.94→21.2→7.94 GeV cycle, is illustrated in Fig. 8 : (i) energy spread, $\sigma_E/E = 2.6 \times 10^{-4}$ at 21.1 GeV and $\sigma_E/E = 8.4 \times 10^{-4}$ back at 7.944 GeV ; (ii) bunch lengthening, $\sigma_l = 2$ mm at 21.1 GeV and $\sigma_l = 2.5$ mm back down to 7.944 GeV ; (iii) normalized horizontal emittance (from zero starting value), namely, $\epsilon_x = 20$ μm at 21.1 GeV (with strong contribution from uncompensated chromatic effects), and $\epsilon_x = 8$ μm back at 7.944 GeV.

Acceptance

The naturally large dynamical acceptance of the linear lattice shrinks with magnet alignment and field defects, this is illustrated in Fig. 9. SR is off in these DA computations, SR causes emittance growth thus reducing the space available for the beam at injection into a recirculation.

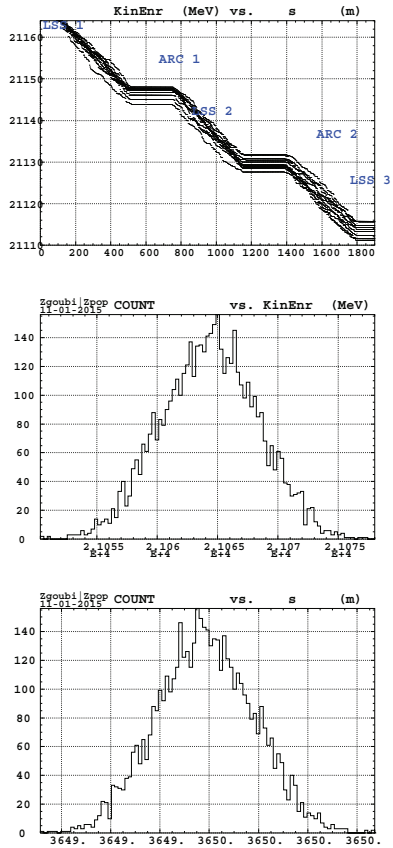

Figure 6: Top : stochastic energy decrease of a few particles over the first 3 arcs at $E_{\rm ref} = 21.164$ GeV. Middle: final spread a 5000 particle bunch after the 21.164 GeV pass, $\frac{\sigma_E}{E_{\rm ref}} = 1.9 \times 10^{-4}$ around $\frac{\overline{\Delta E}}{E_{\rm ref}} = -4.7 \times 10^{-3}$ average energy loss (Eq. 2). Bottom : longitudinal bunch distribution (Eq. 4).

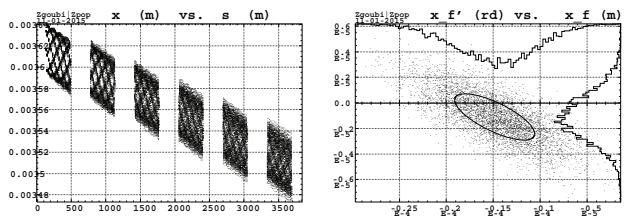

Figure 7: Left : SR loss induced x-drift along the 6 arcs, com-plete ring, $E = 21.164$ GeV, (shown are a few particles in a bunch launched on the LSS axis with zero initial 6-D emittance). Right : a 5000 particle bunch, horizontal phase space after that complete turn, featuring $\overline{x_f} = -15$ μm, $\sigma_{x_f} = 4.3$ μm, $\overline{x'_f} = -1.1.$ μrad, $\sigma_{x'_f} = 1.8$ μrad.

Multipole Defects

Figure 10 illustrates a different way of looking at tolerances, *e.g.* here in the presence of a dodecapole defect in all quadrupoles of the ring (*i.e.*, same working hypotheses as for the bottom Fig. 9) : a 5000-particle bunch is launched with $\epsilon_x \approx \epsilon_y \approx 50\,\pi\mu$m and 10^{-4} *rms* energy spread, for 21 circulations in a complete ring ($6 \times \left[\frac{1}{2}\text{LSS} - \text{DS} - \text{ARC} - \text{DS} - \frac{1}{2}\text{LSS}\right] + \text{Linac}$).

ISBN 978-3-95450-183-0

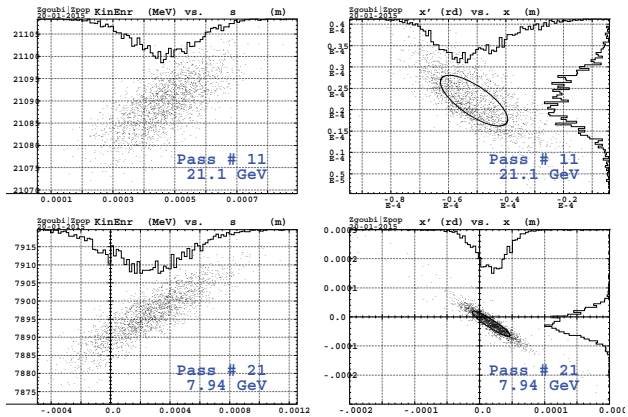

Figure 8: Cumulated effects of SR, in longitudinal (left) and radial (right) phase space, over 21 passes in eRHIC (from 7.944 GeV to 21.164 GeV, and back down to 7.944 GeV). Left plots : energy spread and bunch lengthening. Right plots : horizontal emittance growth

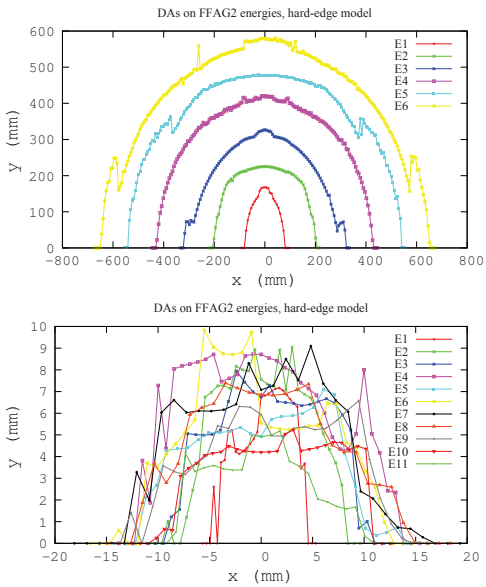

Figure 9: Available injection window into the ring at mid-LSS, for each of the 11 beams, observed at the center of an LSS. Top : defect-free lattice. Bottom : in the presence of dodecapole defect, ±3 Gauss at 1 cm, random uniform.

SR loss is summarily compensated at the linac, bunch position is assumed perfectly corrected at each LSS. Figure 10 shows the emittance evolution, pass after pass, from 7.94 to 21.16 and back to 7.94 GeV. This gives an indication of the maximum tolerable defect, depending on criteria of maximum tolerable emittance, *e.g.* at collision (pass 11) and/or extraction (pass 21).

POLARIZATION

Polarized electron bunch production is based on a Gatling gun, with a polarization of 85-90%. The electron bunch is re-circulated in eRHIC with longitudinal polarization. Spins precess at a rate $a\gamma$ per turn, with an increment of $a\Delta\gamma = 3$ at each 1.322 GeV linac boost, so ensuring the

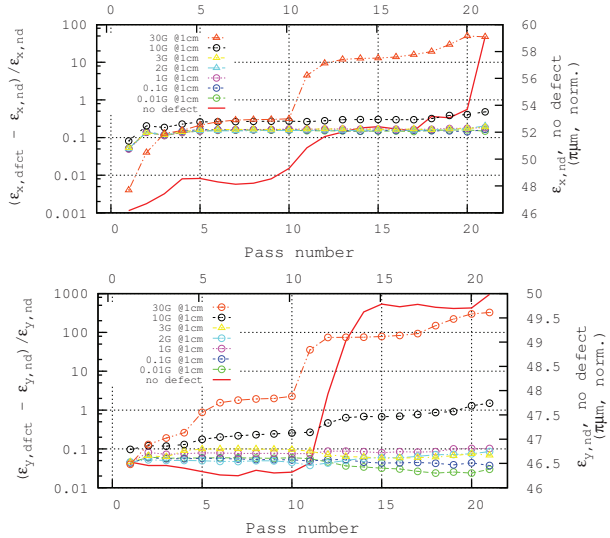

Figure 10: Pass-by-pass evolution of the emittances of a re-circulated bunch, for various dodecapole defect strengths (from 0, to 10 Gauss at 1 cm). Left axis and markers : defect cases. Right axis and red curve : defect-free ring. Top : horizontal, bottom : vertical emittances.

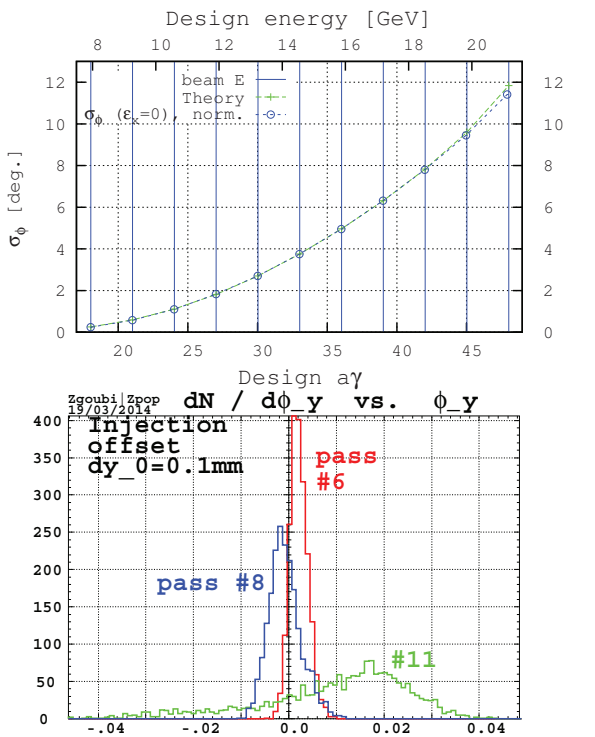

Figure 11: Polarization loss. Top : from energy spread, in-cluding theoretical expectation [8]. Bottom : vertical spin angle spread, in the presence of initial vertical beam jitter.

requested longitudinal spin orientation at the two IPs.

Depolarization mainly stems from energy spread (*e.g.*, a cumulated $2.5\ 10^{-4}$ at 21.2 GeV from SR contribution, see Fig. 8). Spin diffusion resulting from stochastic SR also causes polarization loss, of about 2% at 21.2 GeV. Non-zero vertical emittance, or vertical defects, cause spins to leave the median plane. This is illustrated in Fig. 11.

ISBN 978-3-95450-183-0

Figure 12 monitors the evolution of the polarization and of spin angle spreading, in the conditions of dodecapole error simulations discussed earlier ("Multipole defect" section and Fig. 10). Both quantities appear unchanged in this particular case, compared to the unperturbed optics (cf. σ_ϕ in Fig. 11-left).

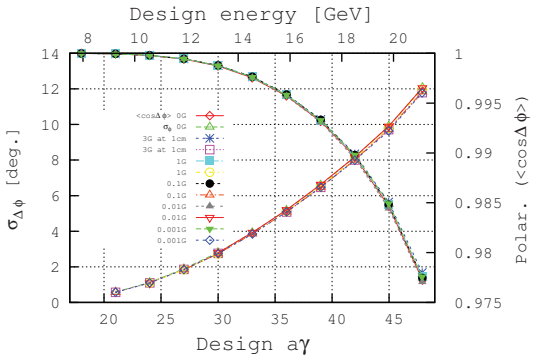

Figure 12: Polarization (right vertical axis) and spin angle spread (left axis) in the presence of dodecapole errors.

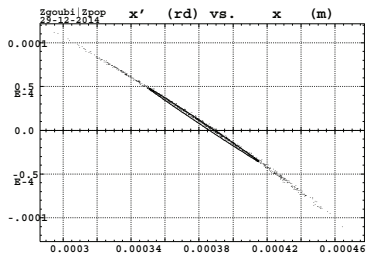

Figure 13: SR induced horizontal phase space portrait, for an initially zero 6-D emittance bunch, as acquired after an 11 GeV pass in the eRHIC ring.

CHROMATIC EFFECTS

Due to the large chromaticity (Fig. 3), any beam misalignment results in phase extent in phase space according to $\Delta\phi = 2\pi\xi\delta E/E$. SR is an intrinsic cause since it introduces both energy spread and beam shift [9], its effect is small however compared to nominal beam emittances, it is illustrated in Fig. 13 which shows the phase-space portrait acquired by a bunch launched with zero emittances and energy spread, after a single 11 GeV pass in the eRHIC ring, assuming a sub-millimeter beam misalignment in the DS regions. Note that here we introduce a measure (used in the following) of that chromaticity related effect in terms of the rms emittance, namely, *surface in phase space* $\epsilon_x = 4\pi\sqrt{< x^2 >< x'^2 > - < xx' >^2}$ (same for (y, y') space), which is thus an *apparent* emittance, including momentum spread induced surface increase.

Since the chromaticity is not corrected in the eRHIC linear FFAG lattice, and given the natural beam energy spread σ_E/E in the 2×10^{-4} range, thus the emittance growth is prohibitive in the absence of orbit correction. This is illustrated, for the horizontal motion, in Fig. 14 which shows the phase space portraits of a 5000-particle bunch at the end of pass 11 (21.2 GeV, collision energy), and at the end

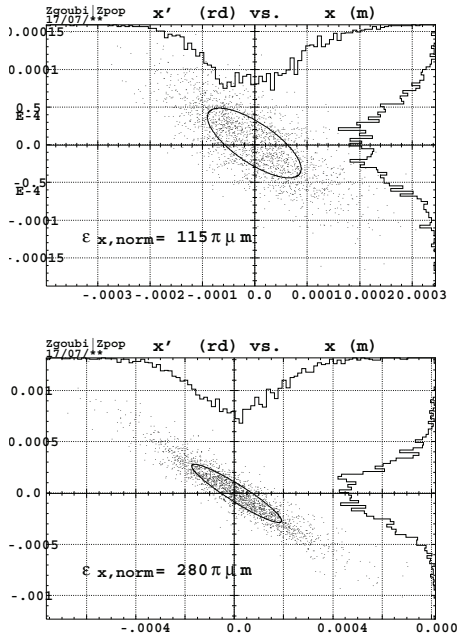

Figure 14: Horizontal phase space portrait of a bunch launched at 7.944 GeV with initial Gaussian *rms* $\epsilon_x \approx \epsilon_y \approx 50\,\pi\mu$m and $dE/E = 0$. Top : end of the 21.2 GeV pass (collision energy), bottom : end of the the decelerated 7.9 GeV last pass.

of pass 21 (back to 7.944 GeV), whereas initial conditions at start, 7.944 GeV, were Gaussian *rms* $\epsilon_x \approx \epsilon_y \approx 50\,\pi\mu$m and $dE/E \in [-10^{-4}, +10^{-4}]$ (random uniform).

Fig. 15 summarizes the overall *apparent* emittance increase, over the 11 accelerated passes (from 7.944 to 21.16 GeV) followed by 10 decelerated passes (from 21.16 back to 7.944 GeV), for a bunch launched at 7.944 GeV with initial Gaussian *rms* $\epsilon_x \approx \epsilon_y \approx 50\,\pi\mu$m and $dE/E \in [-10^{-4}, +10^{-4}]$ (random uniform). In this simulation there is no vertical orbit defect whereas the bunch is (i) experiencing small misalignments in the dispersion suppressors that cause betatron oscillations in the mm range, and (ii) recentered on the theoretical reference orbit once per eRHIC turn, at the linac (*i.e.*, center of an LSS). Bunch distortion in phase space (similar to what is observed in Fig. 13) is at the origin of the steps (local apparent emittance increase) in the region $a\gamma \approx 27$ on the accelerating phase and $a\gamma \approx 38,\ 28$ on the decelerating phase.

Figure 16 shows the much reduced emittance growth in the presence of orbit control, namely here, bunch recentering at each LSS.

Figure 17 is obtained in the case of a vertical orbit defect caused by a small dipole error $a_0 \in [-1, +1]$Gauss, random uniform, injected in all the quadrupoles of the ring. The bunch in this case is recentered at the linac, in both transverse planes, at each turn.

Figure 18 displays the evolution of the polarization (the projection, $\cos(\Delta\phi)$, of the 5000 spins on the average spin direction) and of the spin angle spread σ_ϕ, in the previ-

ISBN 978-3-95450-183-0

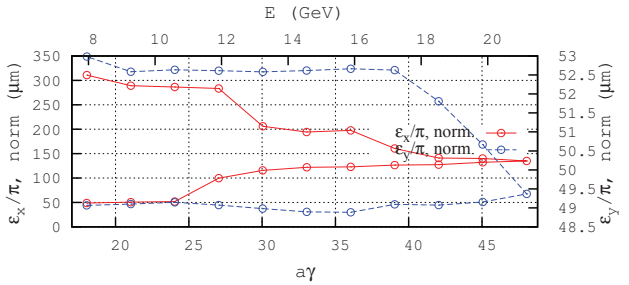

Figure 15: Emittances after each turn. The bunch is recentered once per turn, at the linac.

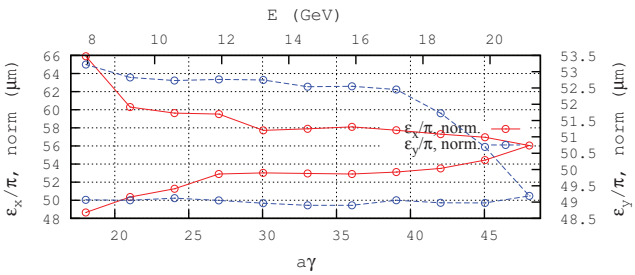

Figure 16: Emittances after each turn. The bunch is recentered at each of the six LSS.

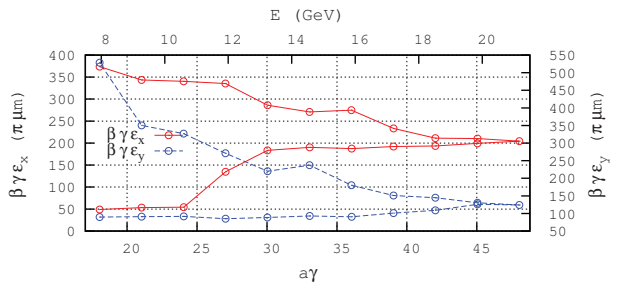

Figure 17: Evolution of the emittances in the presence of vertical orbit defect. Bunch recentered at linac only.

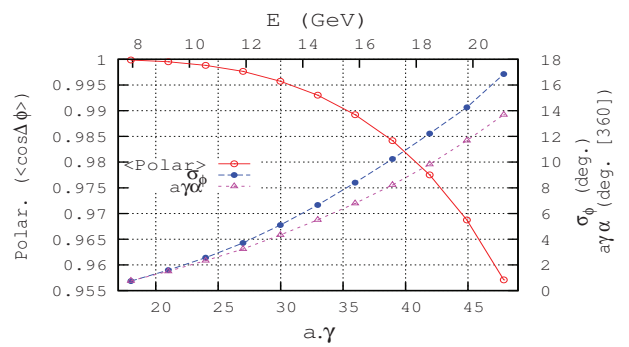

Figure 18: Polarization, spin angle spreading, precession, in the conditions of Figs. 15, 16.

ous conditions of orbit defects : the polarization appears marginally sensible to misalignment effects of this nature and at this level. Note that the number of precessions ($a\gamma$, right vertical axis) slightly differs from an integer value, this is just an indication of a residual effect in the present rough compensation of SR energy loss.

MULTIPLE-BEAM ORBIT CORRECTION

A first approach to multiple-beam orbit correction uses a matching procedure, in which the theoretical FFAG orbit is imposed on the bunch centroid in the arcs, for each energy. The constraint is imposed every 23 cells, this makes 6 such sections to be corrected in a 138 cell arc. That allows 23 variables (H-correctors at quadrupoles) for 22 constraints (x and x' for each one of the 11 energies, in one go). A 50 particle bunch is considered for the matching.

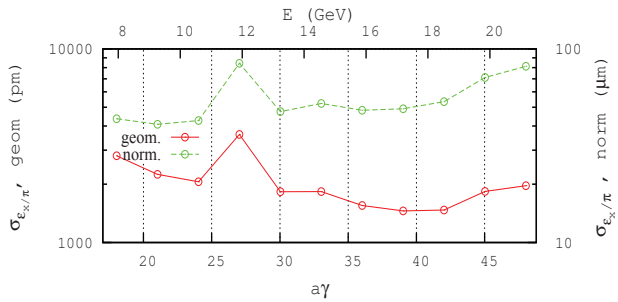

Figure 19: Turn-by-turn evolution of emittances, in the presence of a *corrected* $b_0 \in [-20, +20]$Gauss random defect.

As an illustration, a strong horizontal orbit defect is injected in the arc quadrupoles, namely, a vertical dipole error $b_0 \in [-20, +20]$Gauss (equivalent to misalignment $\Delta x = \pm 40\,\mu$m), random uniform. As a consequence the emittance growth in the absence of correction would be far beyond even what the earlier Fig. 15 shows. Figure 19 displays the evolution of the horizontal emittance after applying that orbit correction scheme in the arcs (orbit correction uses dipole correctors located in drifts between quadrupoles), given initial conditions, at 7.944 GeV, $\epsilon_x \approx \epsilon_y \approx 50\,\pi\mu$m and $dE/E = 0$. This result is promising (the surge at $a\gamma \approx 27$ is again an *apparent* emittance increase resulting from a surge in bunch off-centering at that particular pass/energy in the eRHIC ring).

An option in this method is to apply the constraint cell after cell, in a running mode all around the ring (in both planes in addition, in the presence of both horizontal and vertical multipole defects), until the residual orbit causes tolerable residual emittance growth.

A different type of constraint, rather than the theoretical FFAG orbits, is to request minimal bunch oscillation amplitude in the cells, leaving the average orbit free. This would have the merit of allowing a self-adjustment of the FFAG orbit on the actual bunch centroid energy (which is not the design one, due to SR for instance). This is an on-going study.

APPENDIX

CLOSED ORBIT DEFECTS

Dipolar type of errors due to magnet misalignments and dipole field defects, can be approximated by pairs of identical entrance/exit kicks [4], recalled in Tab. 1, such that

ISBN 978-3-95450-183-0

$\theta_{en}/\theta_{ex} = \Delta(Bl)/B\rho$, with $\Delta(Bl)$ representing the effect of the imperfection.

Table 1: Defect Equivalent Closed Orbit Kicks

	Formulas[(a)]
Horizontal c.o.	
Dipole H kicks	
$\theta/\delta L/L$	$-\theta/(2\cos(\theta/2))$
$\theta/\delta B/B$	$-\tan(\theta/2)$
$\theta/\delta x$	$\sin(\theta/2-\alpha)/(\rho\cos(\alpha))$
$\theta/\delta s$	$\pm\cos(\theta/2-\alpha)/(\rho\cos(\alpha))$
θ/ϕ_z	$\mp\sin(\theta/2)\sin(\theta/2-\alpha)/\cos(\alpha)$
Quad H kicks	
$\theta/\delta x_F$	$K_F^{\frac{1}{2}}\tan(LK_F^{\frac{1}{2}}/2)$
$\theta/\delta x_D$	$-\lvert K_D\rvert^{\frac{1}{2}}\mathrm{th}(L\lvert K_D\rvert^{\frac{1}{2}}/2)$
θ/ϕ_{z_F}	$\pm(LK_F^{\frac{1}{2}}/2\,/\,\tan(LK_F^{\frac{1}{2}}/2)-1)$
θ/ϕ_{z_D}	$\pm(L\lvert K_D\rvert^{\frac{1}{2}}/2\,/\,\mathrm{th}(L\lvert K_D\rvert^{\frac{1}{2}}/2)-1)$
Vertical c.o.	
Dipole V kicks	
$\theta/\delta z$	$\tan\alpha/\rho$
θ/ϕ_x	$\sin(\theta/2)/\theta/2-\cos(\theta/2-\alpha)\cos\alpha$
θ/ϕ_s	$\sin(\theta/2)$
Quad V kicks	
$\theta/\delta z_F$	$-K_F^{\frac{1}{2}}\mathrm{th}(LK_F^{\frac{1}{2}}/2)$
$\theta/\delta z_D$	$\lvert K_D\rvert^{\frac{1}{2}}\tan(L\lvert K_D\rvert^{\frac{1}{2}}/2)$
θ/ϕ_{x_F}	$\pm(L(K_F)^{\frac{1}{2}}/2/\mathrm{th}(LK_F^{\frac{1}{2}}/2)-1)$
θ/ϕ_{x_D}	$\pm(L\lvert K_D\rvert^{\frac{1}{2}}/2/\tan(L\lvert K_D\rvert^{\frac{1}{2}}/2)-1)$

(a) $\mp$ and $\pm$ stand for entrance/exit kick signs, otherwise identical.
(b) Calculated for extreme values K=0.1 m^{-2} and length=1 m.

REFERENCES

[1] E.C. Aschenauer et als., "eRHIC Design Study, Electron-Ion Collider at BNL", arXiv:1409.1633, Sept. 2014.

[2] D. Trbojevic, FFAG Lattice Design of eRHIC and LHeC, EIC 2014 workshop, Newport News (17-21 March 2014).

[3] D. Trbojevic et al., ERL with non-scaling fixed field alternating gradient lattice for eRHIC, IPAC15 Conf. Procs. (Richmond, 2015).

[4] D. Poirier, Etude des défauts de champ magnétiques de MIMAS et correction de la chromaticité de Super-ACO, PhD Thesis, Orsay, 1984.

[5] G. Leleux et al., Synchrotron radiation perturbation in transport lines, Part. Acc. Conf., San Francisco, May 6-9, 1991.

[6] https://oraweb.cern.ch/pls/hhh/code_website.disp_code?code_name=BETA

[7] F. Méot, J. Payet, Simulation of SR loss in high energy transport lines, Rep. CEA DSM DAPNIA/SEA-00-01 (2000).

[8] V. Ptitsyn, Electron Polarization Dynamics in eRHIC, EIC 14 workshop, JLab, 17-21/03/2014.

[9] F. Méot et al., End-to-end 9-D polarized bunch transport in eRHIC, IPAC15 Conf. Procs. (Richmond, 2015).

ISBN 978-3-95450-183-0